Three-dimensional kinetic Monte Carlo simulations of cubic transition metal nitride thin film growth

F Nita, C. Mastail, Gregory Abadias

Three-dimensional kinetic Monte Carlo simulations of cubic transition metal nitride thin film growth

F. Nita, C. Mastail, and G. Abadias*

Institut Pprime, Département de Physique et Mécanique des Matériaux, Université de Poitiers-CNRS-ENSMA, SP2MI, Téléport 2, 86962 Chasseneuil-Futuroscope, France

(Received 6 August 2015; revised manuscript received 10 November 2015; published 10 February 2016)

A three-dimensional kinetic Monte Carlo (KMC) model has been developed and used to simulate the microstructure and growth morphology of cubic transition metal nitride (TMN) thin films deposited by reactive magnetron sputtering. Results are presented for the case of stoichiometric TiN, chosen as a representative TMN prototype. The model is based on a NaCl-type rigid lattice and includes deposition and diffusion events for both N and Ti species. It is capable of reproducing voids and overhangs, as well as surface faceting. Simulations were carried out assuming a uniform flux of incoming particles approaching the surface at normal incidence. The ballistic deposition model is parametrized with an interaction parameter r_0 that mimics the capture distance at which incoming particles may stick on the surface, equivalently to a surface trapping mechanism. Two diffusion models are implemented, based on the different ways to compute the site-dependent activation energy for hopping atoms. The influence of temperature (300–500 K), deposition flux (0.1–100 monolayers/s), and interaction parameter r_0 (1.5–6.0 Å) on the obtained growth morphology are presented. Microstructures ranging from highly porous, [001]-oriented straight columns with smooth top surface to rough columns emerging with different crystallographic facets are reproduced, depending on kinetic restrictions, deposited energy (seemingly captured by r_0), and shadowing effect. The development of facets is a direct consequence of the diffusion model which includes an *intrinsic* (minimum energy-based) diffusion anisotropy, although no *crystallographic* diffusion anisotropy was explicitly taken into account at this stage. The time-dependent morphological evolution is analyzed quantitatively to extract the growth exponent β and roughness exponent α, as indicators of kinetic roughening behavior. For dense TiN films, values of $\alpha \approx 0.7$ and $\beta = 0.24$ are obtained in good agreement with existing experimental data. At this stage a single lattice is considered but the KMC model will be extended further to address more complex mechanisms, such as anisotropic surface diffusion and grain boundary migration at the origin of the competitive columnar growth observed in polycrystalline TiN-based films.

DOI: 10.1103/PhysRevB.93.064107

I. INTRODUCTION

Transition metal nitrides (TMNs) belonging to group IV–VI are a fascinating class of materials which offer, due to their unique combination of metallic, ionic, and covalent bonding, a broad range of applications in manufacturing, semiconductor, optoelectronic, plasmonic, and photovoltaics industries [1–6]. Their refractory character imparts high hardness [7–9], chemical inertness, and thermal stability up to 1000 °C for specific alloys [10–12], which make them widely used as protective and wear-resistant coatings for cutting tools [1]. They also exhibit superconducting properties with critical temperatures reaching 16 and 10.4 K for NaCl-structure NbN and ZrN compounds, respectively [13,14]. Current experimental and theoretical studies focus on improving their mechanical properties by enhancing their toughness while retaining their hardness [15–18]. Microstructural design has proven to be an effective route to achieve such goals, by fine-tuning the elemental composition or tailoring interface properties during thin film synthesis or postgrowth annealing treatments [18–22]. Depending on the deposition conditions and extent of chemical alloying, ternary (or quaternary) TMN thin films may be synthesized, forming either a metastable cubic solid solution with NaCl structure, or a biphase nanocomposite structure [23,24] as a result of segregation of one film forming species [25,26]. In addition to elastic anisotropy at the single-crystal level [27–29], ductility trends in polycrystalline TMNs were shown to be affected by the film microstructure and preferred orientation [18], which can vary significantly with film thickness [30,31].

Most TMN films are nowadays produced from the condensation of vapor fluxes on a solid surface, such as thermal evaporation or sputter deposition, which occur far from thermodynamic equilibrium under reactive or nonreactive atmosphere. Due to their high melting point, TMNs are deposited at relatively low homologous temperature, $T_s/T_m < 0.3$, where T_m is the melting point of the film material and T_s the substrate temperature. This results in limited diffusion of atomic assemblies and generates fine-scale columnar structures, where grains are growing elongated along the growth direction with voided regions in between. The degree of intercolumnar porosity depends on the process conditions. For instance, film densification can be obtained using ion beam assistance, either by applying a bias voltage to the substrate in plasma-based processes or providing an additional, separate ion flux directed towards the growing film surface. The impingement of energetic species contributes not only to increase the adatom mobility but also leads to atomic rearrangements deeper in the film. Highly ionized and pulsed vapor fluxes, like HIPIMS technology [32], offer an alternative way to improve film density and surface smoothness [33].

The most extensive studies have concerned the growth of TiN thin films, which serve as a representative archetype of TMN thin film growth. Recent studies by Mahieu and

*Corresponding author: gregory.abadias@univ-poitiers.fr

Depla [34,35] have addressed the phenomenology of TiN growth by reactive sputter deposition and categorized the different microstructures, surface morphologies, and preferred orientations in an extended structure zone model (SZM) [34]. For films developing a zone-T columnar microstructure, characterized by the competitive growth of (111) and (100) planes, characteristic "V-shaped" columns develop with increasing thickness and emerge at the surface with oriented facets. These structural features are the result of kinetic limitations: grains with the largest rate along the substrate normal will overgrow all other grains. More particularly, the anisotropy in titanium adatom mobility, and nature of incoming nitrogen flux (atomic N versus molecular N_2) and film forming species (Ti and N adatoms versus TiN dimers), have been shown to be decisive in governing the texture development [35,36]. This evolutionary growth regime is most frequently accompanied by a crossover of preferred orientation with film thickness [30]. For deposition at higher homologous temperatures, grain boundaries are no longer immobile and restructuring may occur. Consequently, the film preferred orientation is thermodynamically driven, resulting in the formation of straight columns extending throughout the entire film thickness and oriented with the plane of lowest surface energy parallel to the substrate, i.e., (001) in the case of TiN [37]. These changes in preferred orientation and structural attributes significantly impact the stress state [38,39] and mechanical properties [40] of TiN coatings. For ternary TMNs, the situation is even more complex as the incorporated alloying species affect not only the Ti and N surface diffusion but can contribute to defect creation by momentum transfer [23,41].

The control of thin film microstructure and surface morphology is therefore essential in order to go a step further in the improvement of the physical and mechanical properties of TMN thin films. However, this is a challenging task as film microstructures are depending on a rather large number of interrelated factors. While the influence of experimental parameters, such as substrate temperature, deposition rate, working pressure, characteristics of the vapor flux (nature of film forming species, ion-to-neutral ratio, kinetic energy, and angular distribution of incoming particles), and geometry of the deposition chamber on the resulting film microstructure and properties can be routinely apprehended, these hardly permit an accurate control of the elementary, atomic-level processes governing the microstructure evolution during growth, such as plasma/surface interaction, surface diffusion, atom impingement, etc. This stimulates the need for the development of comprehensive and predictive models relying on numerical simulations and implementing a multiscale approach able to account for detailed atomistic mechanisms over a realistic system size (several tens of nm^3) and time scale (minutes to hours) comparable to experiments.

Kinetic Monte Carlo (KMC) simulations are successfully employed to predict thin film growth morphologies on technologically relevant time and length scales. They can reproduce the stochastic nature of the growth process and allow for the implementation of a variety of atomistic processes, whose rates are ideally obtained from more detailed and accurate calculations, like molecular dynamics (MD) or first principles methods based on density functional theory (DFT). Several KMC models have been proposed in the literature over the last decades [42–47], based on two-dimensional (2D) or three-dimensional (3D) rigid lattices, some even accounting for the impact of energetic particle [48] but none of them have specifically addressed the growth of TMNs during reactive sputtering, where it is required to consider both metal and nitrogen species for deposition and diffusion events. Recent MD simulations by Sangiovanni *et al.* [49] on the growth dynamics of TiN (001) surface have confirmed the significant difference in migration rates between Ti and N species, as well as the implication of TiN_2 trimers in transport properties.

In this paper, we report the initial results of KMC modeling of TiN growth morphology based on a 3D rigid lattice with a predefined orientation. It constitutes the first step for paving the whole sputter-deposition process, from ion-target interaction (provided by SRIM code [50]) and transport in the gas phase (provided by SIMTRA code [51]), up to the growth itself. The choice of TiN is motivated by the fact that it corresponds to the most documented system in the literature, especially because surface diffusion and lateral binding energies, which are necessary inputs to parametrize the model, have been computed by DFT and/or MD, supporting reliable and quantitative predictions. TiN can also be considered as a model system, being the prototype system of TMN compounds crystallizing in the cubic NaCl structure, which renders to our model a general character. Our KMC model includes both diffusion and deposition events of Ti and N species and different directionalities of arriving particles spanning both thermal evaporation and low-energy sputter-deposition conditions. Two diffusion models have been considered, based on the different ways to compute the diffusion barrier. The influence of diffusion models as well as main deposition parameters affecting surface morphology and microstructural evolution with film thickness, such as deposition rate and substrate temperature, are presented and discussed. Dynamic scaling exponents are utilized for a quantitative characterization of the obtained results, assuming a self-affine surface growth [52].

II. COMPUTATIONAL METHOD

A. Description of the 3D rigid lattice

The TiN system has a cubic B1 (NaCl-type) structure with a bulk lattice parameter $a_0 = 0.424$ nm [53]. A single 3D rigid lattice obtained by the superposition of two face-centered cubic (fcc) sublattices, metal and nitrogen sublattices [see Fig. 1(a)], and oriented along the crystallographic reference frame, has been used in simulations. Considering L_x as being the extension of the system in the x direction, the distance between two successive lattice sites is set to half of the TiN lattice parameter ($a_0/2$); i.e., the number of elementary cells along x direction is $N_x = 2L_x/a_0$ (same on y, z for L_y, L_z). Periodic boundary conditions have been used on the x and y directions.

For a given sublattice site, its nearest neighbors (nn) sites belong to the complementary fcc sublattice and its next-nearest neighbors (nnn) sites belong to the same fcc sublattice, the maximum number of nn and nnn sites being six and 12, respectively [see Fig. 1(a)].

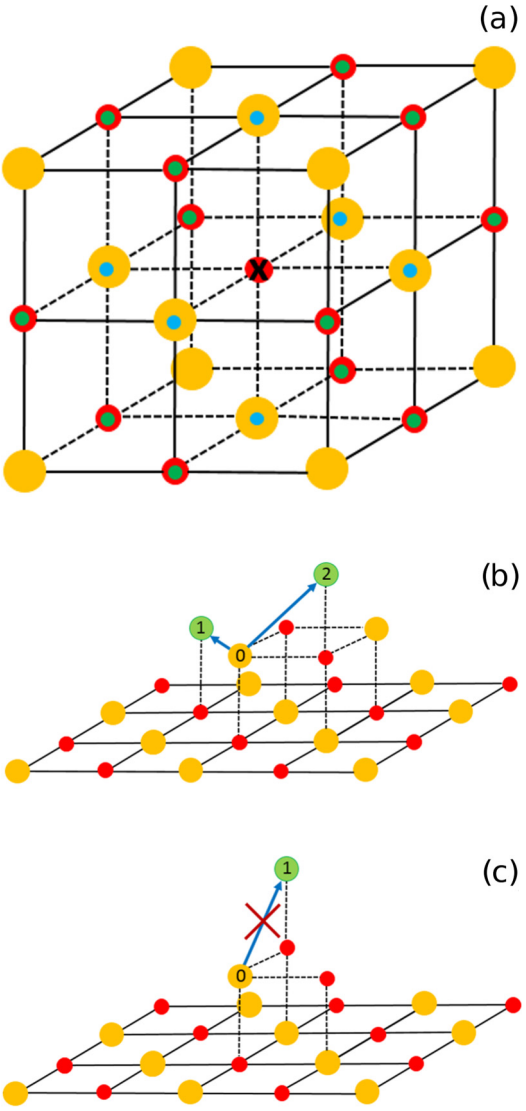

FIG. 1. (a) Representation of the NaCl-type lattice cell of TiN: Ti atoms (large yellow spheres) and N atoms (small red spheres) occupy their own fcc sublattice positions. Two possible final sites (b) and a forbidden final site (c) for a diffusing Ti atom, according to the surface contact rule.

B. KMC model

1. Methodology

KMC simulations of a stoichiometric TiN system have been done at different temperatures T (K), and for different deposition rates F [monolayers (ML)/s)], using the above described 3D lattice. The KMC model takes into account two kinds of elementary events: deposition and 3D diffusion. Similarly to the works reported in Refs. [42,47,48,54], we used the assumption that the deposition and diffusion events are two completely independent events.

Considering the deposition rate F as being constant, the time interval between two successive deposition events τ depends only on the deposition rate and system dimensions: $\tau = 1/(F \times N_x \times N_y)$. The deposition event is then a periodic event and the total time t_{tot} of the system is continuously counted from the very beginning of the simulation as the total number of the deposited particles, N_{dep}, multiplied by τ, $t_{\text{tot}} = N_{\text{dep}}\tau$.

A deposition timer t_0 is reset to 0 after each deposition event, and a certain number of diffusion processes can happen until the arrival of a new particle. Each modification of the system configuration as a result of a diffusion process takes a specific, computed time Δt. After each diffusion event, t_0 increases by Δt: $t_0 = t_0 + \Delta t$. If $t_0 \geqslant \tau$, a new particle is added to the system; t_{tot} becomes $(N_{\text{dep}} + 1)\tau$.

To choose a diffusion event a two-step procedure has been implemented. All possible diffusion processes are classified into different energy classes according to their specific diffusion barrier E_j. All N_j processes belonging to the class j have the same rate given by the Arrhenius law: $r_j = \nu^* \exp(-E_j/kT)$. The total rate corresponding to the class j is $R_j = N_j \times r_j$, and the total rate of all possible diffusion events in the system is $R = \sum(R_j)$. We firstly choose a diffusion class j, the probability being proportionally to its own rate R_j, then we choose with an equal probability one of the N_j processes belonging to this energy class. The time spent to change the configuration of the system performing a diffusion event is $\Delta t = 1/R$, and this Δt is added to t_0 as described before.

A simulation stops when the height of the deposited structure equals L_z (following a deposition or a diffusion process) or the number of atoms (monolayers) given as an input parameter has been reached.

2. Diffusion models

In the present work, we consider only the diffusion of a single atom (either N or Ti), the diffusion of dimers or larger aggregates being neglected, as their mobility is much lower [49]. We emphasize the 3D characteristic of the diffusion event: considering a diffusing atom, such event is allowed, obeying certain conditions, towards any of its 12 nnn sites; i.e., there are 12 potential elementary diffusion processes associated to a given site. For a given particle, diffusion is limited to its own sublattice, meaning that substitutional or interstitial defects are forbidden. An elementary diffusion process is defined by its initial site p, the diffusion direction, and the corresponding energy barrier.

The diffusion process will obviously take place when the initial site is occupied and the final site is empty. However, to ensure contact with the surface, we consider that each occupied site (each particle) must fulfill a specific rule, that we call *the surface contact rule*, defined by minimum numbers $N_{\text{nn}}^{\text{min}}$ and $N_{\text{nnn}}^{\text{min}}$ of occupied nn and nnn sites, respectively. Here, we impose $N_{\text{nn}}^{\text{min}} \geqslant 1$ and $N_{\text{nnn}}^{\text{min}} \geqslant 1$. A particle that obeys strictly the surface contact rule is considered as being an adatom.

Different diffusion models can be considered based on the different manners to compute the diffusion barrier for an elementary diffusion process and/or obeying a specific surface contact rule, as described above. We chose to implement a bond-counting model [43,55,56]. For a particle occupying a given site p, its total interaction energy, E_{tot}, is computed as the sum of the number of nn and nnn occupied sites of the p site multiplied by the corresponding interaction energies (E_{nn} and E_{nnn}, both positives), according to

$$E_{\text{tot}} = -(N_{\text{nn}}E_{\text{nn}} + N_{\text{nnn}}E_{\text{nnn}}). \quad (1)$$

TABLE I. Parameters used for KMC models of TiN thin film growth: activation barrier for surface diffusion (E_b), number of minimum nearest (N_{nn}^{min}) and next-nearest (N_{nnn}^{min}) neighbors to ensure surface contact rule. Lateral binding energies, $E_{Ti\text{-}Ti}$, $E_{Ti\text{-}N}$, and $E_{N\text{-}N}$, were taken from DFT calculations from Gall *et al.* [36]. E_{tot} is the total interaction energy given by Eq. (1).

	E_b	E_0^{Ti} (eV)	E_0^{N} (eV)	E_{nn} $E_{Ti\text{-}N}$ (eV)	E_{nnn} $E_{Ti\text{-}Ti}$ (eV)	E_{nnn} $E_{N\text{-}N}$ (eV)	Surface contact rule N_{nn}^{min}	Surface contact rule N_{nnn}^{min}	nn and nnn included into E_0 value[a] N_{nn}^{0}	nn and nnn included into E_0 value[a] N_{nnn}^{0}
Model 1	$E_0 + N'_{nn}E_{nn} + N'_{nnn}E_{nnn}$	1.0	1.0	2.85	1.12	2.12	1	1	1	4
Model 2	$E_0 + \Delta E_{tot}$ if $E_{tot}^f > E_{tot}^i$	1.0	1.0	2.85	1.12	2.12	1	1	1	1
	E_0 if $E_{tot}^f \leqslant E_{tot}^i$						1	3	1	3

[a]See text.

Using the above described 3D lattice, we have performed simulations using the following two different diffusion models:

Model 1: The diffusion activation barrier, E_b, is computed taking into account the configuration of the initial site, i.e., $E_b = E_0 + N'_{nn}E_{nn} + N'_{nnn}E_{nnn}$, where E_0 is the diffusion barrier of an adatom diffusing onto a given orientated terrace, and so accounts for the interaction with all occupied nn (N_{nn}^0) and nnn (N_{nnn}^0) belonging to this surface. N'_{nn} and N'_{nnn} correspond to lateral neighbors (i.e., those nn and nnn occupied sites that do not belong to the terrace below) defined by $N'_{nn} = N_{nn} - N_{nn}^0$ and $N'_{nnn} = N_{nnn} - N_{nnn}^0$, so that $N'_{nn}E_{nn} + N'_{nnn}E_{nnn}$ accounts for the lateral binding energy. Note that $N_{nn}^0 \geqslant N_{nn}^{min}$ and $N_{nnn}^0 \geqslant N_{nnn}^{min}$. Such diffusion model has been already used to perform KMC simulations of polycrystalline thin film deposition and to study the electromigration in the deposited 3D structures [43,57].

Model 2: The diffusion activation barrier is computed taking into account the difference between the energy of the system after and before the jump (ΔE_{tot}). The activation barrier is $E_b = E_0 + \Delta E_{tot}$, if $E_{tot}^f > E_{tot}^i$ and $E_b = E_0$, and if $E_{tot}^f \leqslant E_{tot}^i$, where E_{tot} is computed from Eq. (1). Here, superscripts i and f refer to initial and final positions, respectively. In this case E_0, called migration energy, does not have the same meaning as in model 1. A detailed explanation of it can be found in Ref. [54].

Both diffusion models obey the detailed balance, all movements in the system being reversible [58]. However, if we do not impose a surface contact rule, the detailed balance is broken.

The isotropic/anisotropic character of surface diffusion depends on the crystallographic surface properties, e.g., Cu on Cu(110) where diffusion is faster along the atomic row aligned along ⟨110⟩ than across them [59]. For TiN, there is experimental evidence that columns tend to expose their crystal habits along [001], [111], or [110], depending on the deposition conditions [34,35]. TiN being a binary system, we must distinguish between N and Ti diffusing species, with corresponding E_0^{Ti} and E_0^{N} values. E_0^{Ti} and E_0^{N} have been computed by DFT calculations for the {001} [36], {111} [60], and {110} TiN surfaces [61]. These calculations confirmed the dependence on the surface orientation of the energy barrier for the diffusion of both adatom species. Additional DFT calculations performed by Gall *et al.* [36] on TiN(001) surface provided energy values corresponding to Ti-Ti, Ti-N, and N-N interactions, values that we used as binding energies. Different diffusion mechanisms at steps on TiN(001) surface have been identified and their corresponding activation energies have been computed by MD calculations [62,63]. However, we did not take explicitly into account at this stage the crystallographic diffusion anisotropy intrinsic to the real TiN system or any Ehrlich-Schwoebel barrier. In both models 1 and 2, E_0^{Ti} was taken as the average of all the available computed values (a value of 1.0 eV is retained), and we assumed $E_0^{N} = E_0^{Ti}$.

For model 1, because the DFT computations for E_{nn} and E_{nnn} have been done on TiN(001)surface, we choose $N_{nn}^0 = 1$ and $N_{nnn}^0 = 4$, this corresponding to an adatom on TiN(001) surface. In this case, if $N_{nnn} \geqslant N_{nnn}^0$ then $N'_{nnn} = N_{nnn} - N_{nnn}^0$ and if $N_{nnn} < N_{nnn}^0$ then $N'_{nnn} = 0$. Within model 2, different surface contact rules can be considered as well, and we will report and compare results for $N_{nn}^{min} = 1$ and $N_{nnn}^{min} = 1$, and $N_{nn}^{min} = 1$ and $N_{nnn}^{min} = 3$; for both situations, $N_{nn}^0 = N_{nn}^{min}$ and $N_{nnn}^0 = N_{nnn}^{min}$. The characteristics of both considered models and input parameters used in each case are summarized in Table I.

It is important to notice that model 1 is an isotropic diffusion model since the diffusion barrier depends only on the configuration of the initial site. This characteristic is independent of the imposed surface contact rule. However, model 2 includes intrinsic diffusion anisotropy due to the fact that to compute the diffusion barrier E_b for an elementary diffusion process both initial and final configurations are taken into account. This is illustrated in Figs. 1(b) and 1(c). Figure 1(b) shows two possible final sites for a diffusing Ti atom belonging to an island on top of a (001) terrace. Its initial position, site 0 has three nn occupied sites, among which one is in the terrace below, and five nnn occupied sites, among which four are in the terrace below. The site 1 has two nn occupied sites (one in the layer below and one in the island) and four nnn occupied sites (all in the terrace below), while site 2 has one nn and two nnn occupied sites (both in the island). Considering the diffusion model 1 both diffusion processes are characterized by the same diffusion barrier: $E_0^{Ti} + 2E_{Ti\text{-}N} + E_{Ti\text{-}Ti}$, while for model 2 one obtains: $E_0^{Ti} + E_{Ti\text{-}N} + E_{Ti\text{-}Ti}$ and $E_0^{Ti} + 2E_{Ti\text{-}N} + 3E_{Ti\text{-}Ti}$ for diffusion to sites 1 and 2, respectively. Figure 1(c) shows a forbidden final site for a diffusing Ti atom: if atom at site 0 jumps to site 1 then it will have only one nn (and zero nnn), which breaks the surface contact rule.

3. Ballistic deposition model

As in the diffusion models, the deposition of aggregates having a dimension larger than 1 is forbidden and only single particles, either Ti or N, can be deposited at a time. The nature of the deposited particle can be selected with a certain probability according to the system stoichiometry. The deposition rate, F, is constant and a particle can be added to the system on a site belonging to a sublattice chosen according to the nature of the particle (see Sec. II A). The particle trajectories can have different orientations in respect with the substrate surface normal, orientations controlled by the polar and azimuthal angles (θ,ϕ). Only results obtained at normal incidence will be reported in this paper. However, for the sake of clarity we will describe in the following the deposition procedure corresponding to the general case.

At each deposition step, a launching point is randomly selected above the surface, having initial (x_i, y_i, z_i) coordinates. We assume a ballistic deposition process where the trajectory is computed along the (θ,ϕ) direction, and all sublattice sites (according to the depositing particle nature) belonging to a cylinder along the computed trajectory are selected as being potential available sites for deposition. The cylinder radius, r_0, can be controlled and this parameter mimics a collision parameter/interaction distance (see Fig. 2). In this way, we aim at modeling more realistic deposition conditions where particles get trapped due to short-range interactions with the surface by opposition to classical ballistic models, where the species follow straight-line trajectories until their impingement on a surface site. This approach is equivalent to the concept of the surface trapping mechanism proposed by Alvarez *et al.* [64] in their KMC model.

The particle will attach to the first encountered stable deposition site, a stable deposition site being an empty site obeying the surface contact rule (same as in a diffusion event). At an instantaneous position of the incoming particle on its trajectory, the potential stable sites are searched for inside a hemisphere having its center at the particle position and radius equal to r_0, oriented in the forward direction. If there are several stable deposition sites in this hemisphere, but with different E_{tot}, then the most energetically stable of them, having E_{tot} minimal, is chosen; if there are several sites having the same E_{tot} minimal energy, any of them can be chosen with equal probability.

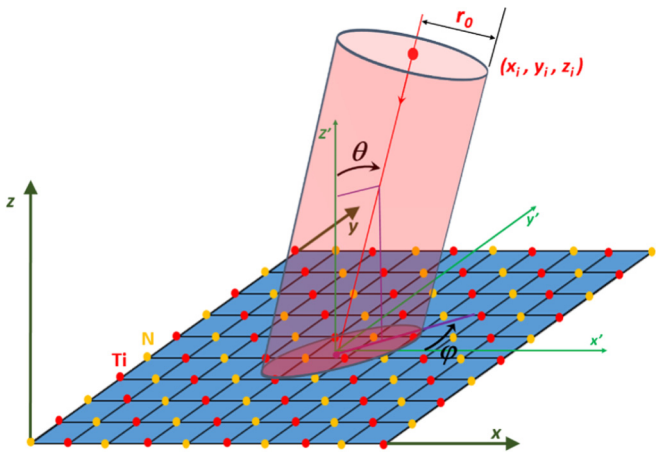

FIG. 2. Ballistic deposition model: starting from a random chosen initial position (x_i, y_i, z_i) the particle trajectory can have different orientations (θ,φ) with respect to the normal of the substrate surface. The selection of a good deposition site is done, according to a specific energy minimization procedure, using the lattice sites belonging to a cylinder having radius r_0 and drawn around the computed trajectory of the particle.

On its way to the substrate, an incoming particle can encounter a "compact surface." This happens when all potential available deposition sites belonging to the above mentioned hemisphere are occupied. In such a case, the particle stops to go further and searches for a stable deposition site on its specific sublattice. The search is extended until the second-order coordination sphere of the last visited site before the particle meets the compact surface. This procedure corresponds to a local rearrangement in the neighborhood of the initial impact position, typically favored in physical vapor deposition processes. Even thermalized particles will be accelerated in the vicinity of the surface, gaining kinetic energy of about 1–2 eV (as part of the latent heat released during condensation) [48,65].

It must be noticed that the substrate surface is considered as the last compact surface that an arriving particle can meet and, eventually, attach to. If a stable deposition site still cannot be found then a new incoming particle is chosen and its corresponding trajectory is computed from new initial position (x_i, y_i, z_i) and orientation (θ,ϕ) angles.

It must be mentioned that, because of the implemented deposition model and use of r_0 parameter, some supplementary surface mechanisms can be considered as being taken into account, even if not explicitly: a change in the initial velocity orientation toward the surface of the deposited 3D structure (due to attractive force exerted by surface atoms) and a possible reflection when the incoming particle reaches a compact surface [48].

III. RESULTS AND DISCUSSION

We present in this section KMC simulations for a system size of $L_x = L_x = L_z = 21.2$ nm corresponding to deposition of several tens up to a maximum of 100 TiN monolayers, depending on the compactness of the TiN film. To ensure that the obtained growth characteristics were not biased by the box size, other simulations were performed on larger computational boxes, and yielded similar results. To account for the compactness of the deposited structures we introduced a compactness order parameter, C, defined as the ratio between the number of particles having six nn occupied sites and the total number of deposited particles. The compactness order parameter reflects quite well what we can observe by a simple visual inspection of the simulated structures.

To describe and quantify the time evolution of the growing 3D system we used as indicators the interface width or rms surface roughness, w, defined by

$$w^2 = \langle [h(\boldsymbol{r},t) - \bar{h}(t)]^2 \rangle, \tag{2}$$

where $h(\boldsymbol{r},t)$ is the surface height at time t and at a position given by $\boldsymbol{r} = (x,y)$, $\bar{h}(t)$ is the average height at time t, and $\langle \cdots \rangle$ denotes the statistical average over the entire surface; the equal-time height difference correlation function $G(\boldsymbol{r})$

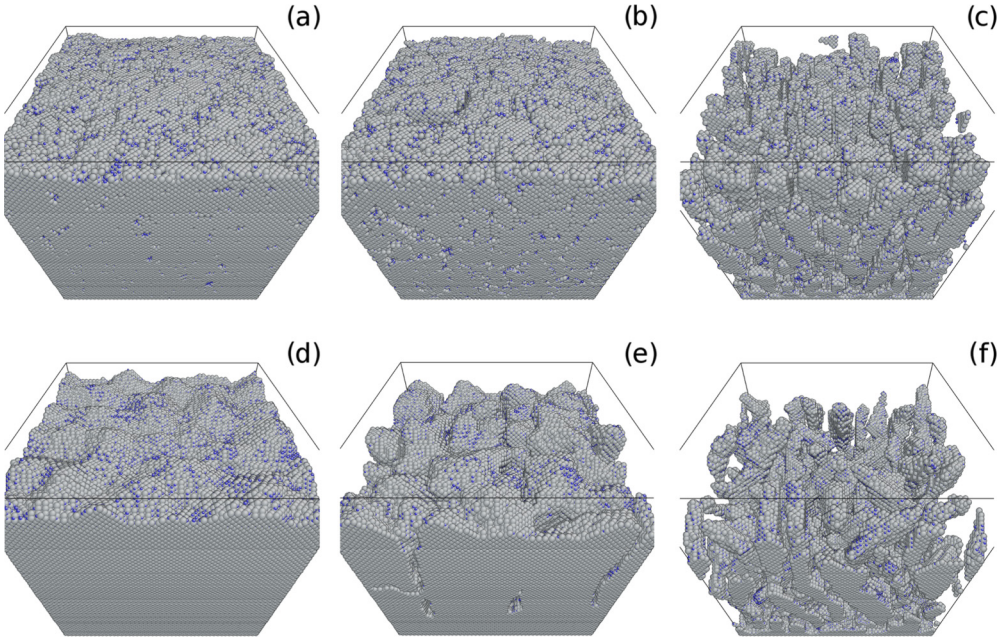

FIG. 3. Snapshots of the simulated TiN film growth structures corresponding to diffusion model 1 (a–c) and model 2 (d–f), at $T = 500$ K, $F = 1$ ML/s, $N_{nn}^{min} = 1$ and $N_{nnn}^{min} = 1$, and different values of the interaction parameter r_0: $\sqrt{2}/2$ (a,d); $\sqrt{2}$ (b,e); and $2\sqrt{2}$ (c,f). The simulation box dimensions are $N_x = N_y = N_z = 100$ (see Ref. [76]).

given by

$$G(\boldsymbol{r}) = \langle [h(\boldsymbol{r}+\boldsymbol{r}',t) - h(\boldsymbol{r}',t)]^2 \rangle, \quad (3)$$

and the normalized layer density $\rho(z,t)$ defined as the ratio of all occupied sites in a plane parallel to the substrate at a given z coordinate to the total number of sites ($N_x \times N_y$) in the plane. If w provides information about the apparent surface of the system, the quantity $\rho(z,t)$ describes rather a volume property—the density profile along z, which can be used to determine the layer-by-layer system porosity [66].

Results will be shown for different substrate temperatures (300–500 K), deposition rate (0.1–100 ML/s), and interaction distance r_0 ($\sqrt{2}/2 - 2\sqrt{2}$, expressed in $a_0/2$ unit) for stoichiometric TiN films deposited at normal incidence.

A. Parameters affecting film morphology

1. Diffusion model and interaction parameter

To discuss the influence of diffusion models on the resulting TiN growth morphology, KMC results are first shown at $T = 500$ K (Fig. 3), at which diffusion events are significant (eight diffusion events/deposited atom) compared to lower substrate temperatures. Snapshots of the final TiN film microstructures obtained for different r_0 values are reported in Figs. 3(a)–3(c) and 3(d)–3(f) for models 1 and 2, respectively. Comparing the two models at a given r_0 value, one can see that smoother surfaces are obtained for model 1. The tendency to develop straight columns is found for model 1, while more inclined columns and protuberances are formed when using model 2. This is especially visible at larger r_0 values [Figs. 3(c) and 3(f)]. A closer inspection of Fig. 3(c) reveals that the microstructure consists of well separated square-shaped vertical columns with {100} facets. This is better visualized in Fig. 4(b), where the inset shows a magnified view of the column tops, terminated by nonpolar (001) surfaces. This situation would correspond to a cube-on-cube epitaxial growth, where all columns are oriented along [001] with their top surfaces parallel to the substrate.

Model 2 results in denser film microstructures, with the formation of fully dense films at $T = 500$ K and $r_0 = \sqrt{2}/2$ [Fig. 3(d)]. In this case, the surface is characterized by the presence of mounds with typical lateral size of ~5 nm. With increasing values of r_0 [Figs. 3(d)–3(f)], the compactness decreases from 0.99 to 0.63, associated with a kinetic roughening (w increases from 4 to 36 Å). The surface contact rule has marginal influence on the surface morphology at this temperature (see Table II). The formation of denser films can be explained by the fact that adatoms diffusing to higher coordination number sites experience a lower barrier energy (1.0 eV) compared to model 1. For both models, the formation of voids and overhangs is favored at larger r_0 values, as a result of the shadowing effect. This phenomenon will be additionally discussed later for model 2. Interestingly, one observes the formation of different crystallographic facets, despite the use of a single-oriented lattice. A typical example is shown in the inset of Fig. 4(c), evidencing a N-terminated {111} surface with hexagonal stacking. Other surface orientations, such as {110} or {001}, are also observed in the simulation box when using model 2, while only (001)-oriented surfaces were formed with model 1. As mentioned in Sec. II B, model 2 includes an *intrinsic* (local) diffusion anisotropy and the corresponding results are in qualitative good agreement with experimental findings on magnetron sputter-deposited TiN thin films, see Fig. 4(a). Such faceted growth front is characteristic of high-mobility deposition conditions [750 K for the case shown in Fig. 4(a)], where surface diffusion is thermally activated.

TABLE II. Results overview for diffusion model 2 using normal deposition with $F = 1$ ML/s and different values of interaction parameter r_0, temperature T, and surface contact rule conditions. The simulation box dimensions are $N_x = N_y = N_z = 100$. Each cell contains from top to down: the time to reach L_z, t_e (s), the rms surface roughness, w (Å), and the compactness parameter, C.

		$r_0(a_0/2$ units)					
		$\sqrt{2}/2$		$\sqrt{2}$		$2\sqrt{2}$	
T (K)		$N_{nn}^{min}=1$ $N_{nnn}^{min}=1$	$N_{nn}^{min}=1$ $N_{nnn}^{min}=3$	$N_{nn}^{min}=1$ $N_{nnn}^{min}=1$	$N_{nn}^{min}=1$ $N_{nnn}^{min}=3$	$N_{nn}^{min}=1$ $N_{nnn}^{min}=1$	$N_{nn}^{min}=1$ $N_{nnn}^{min}=3$
300	t_e	45.34	86.38	22.45	54.81	8.98	22.83
	w	7.59	3.94	13.79	6.99	47.42	37.02
	C	0.16	0.74	0.02	0.25	0.02	0.21
400	t_e	60.74	88.42	25.81	58.48	9.54	22.90
	w	9.01	5.05	19.44	9.69	56.03	41.53
	C	0.67	0.94	0.27	0.60	0.11	0.34
500	t_e	91.60	91.94	76.28	79.67	29.31	33.68
	w	4.43	4.48	13.06	11.80	36.00	33.37
	C	0.99	0.99	0.90	0.92	0.63	0.65

The facets that form the crystal habit correspond to the planes of lowest crystallographic growth rate, which in turn depends on the number of nearest neighbors offered by the growing plane to the incoming species [34]. For instance, {100} facets are expected to develop under plasma conditions where reactive gas is in the molecular state (N_2). This results in {100} faceting and [111] out-of-plane preferred orientation. Conversely, {111} faceted grains will form under atomic nitrogen condition, and texture will develop along the [100] growth direction. This latter situation is observed when growing TiN films at 750 K under metallic sputtering mode (low N_2 partial pressure), where pyramids with fourfold symmetry tilted facets with respect to the substrate can be clearly distinguished in the scanning electron microscope (SEM) image of Fig. 4(a). Note also that flat columns are formed, which may correspond to [001]- or [110]-oriented surfaces parallel to the substrate, as it is difficult to unequivocally make a statement about their square or rectangular shape.

For both models, the influence of the interaction parameter r_0 on the resulting film porosity is the same. The decrease in r_0 reduces the voids' size and voids' density. This is a direct consequence of the deposition model: larger r_0 values correspond to a higher probability for a particle to stick laterally on an existing surface. This prevents them from reaching exposed surfaces placed at lower heights. Therefore, even a normal incidence deposition at large r_0 resembles more of a "hit and stick" ballistic deposition process, which favors the formation of porous TiN morphologies, with overhangs and voided regions. Conversely, decreasing r_0 would reflect deposition conditions under a more energetic particle bombardment. Although the deposited energy of the incoming particles flux is not yet included explicitly in the KMC code, the r_0 parameter seemingly captures its effect, at least qualitatively.

In the present work the crystallographic diffusion anisotropy is not explicitly taken into account, but it can be concluded that the faceting phenomenon is well reproduced when considering the local anisotropy, and we cannot neglect it when trying to explain the structural properties of the TiN system. Therefore, in what follows, we will restrict the discussion of the results obtained using model 2 only.

2. *Substrate temperature*

Figure 5 shows the typical TiN microstructures predicted at substrate temperatures of 300, 400, and 500 K, with the conditions $F = 1$ ML/s, $N_{nn}^{min} = 1$ and $N_{nnn}^{min} = 3$, $r_0 = \sqrt{2}$ being fixed. As expected, the film compactness increases from 0.25 to 0.92 with increasing temperature due to thermally activated surface diffusion processes, which favor local atomic rearrangement. This is reflected also by the time required to reach the L_z dimension of the simulation box by the deposit (see also Table II). In the same time, the surface roughness increases from ~7 to 12 Å, as a result of surface faceting favored at higher temperature. One can notice in Fig. 5(c) the presence of tilted columns and the formation of occluded voids, predominantly due to the shadowing effect. If we compare Figs. 5(c) and 3(e), one can see that a slightly denser microstructure is favored when prescribing a more stringent surface contact rule $N_{nn}^{min} = 1$ and $N_{nnn}^{min} = 3$ instead of $N_{nn}^{min} = 1$ and $N_{nnn}^{min} = 1$. This is more evidently the case at lower temperatures, see Table II.

3. *Deposition rate*

We also investigated the influence of the deposition flux F on the resulting TiN microstructures. At $T = 500$ K and $r_0 = \sqrt{2}$, increasing F from 0.1 to 100 ML/s results in a significant decrease of the film compactness from 0.90 to 0.50, while the surface roughness varied in a nonmonotonous way from ~16 to 18 Å. At low deposition rate, atoms have sufficient time to diffuse, resulting in dense microstructures but also in the formation of grains with larger facets. Increasing the deposition rate increases the nucleation centers' density for atom aggregation, and leads to the development of porous (fibrous) morphologies.

B. Time-dependence morphological evolution and scaling behavior

Different models have been proposed in the literature to understand the physics associated with the formation and evolution of a dynamic surface/interface, such as during the

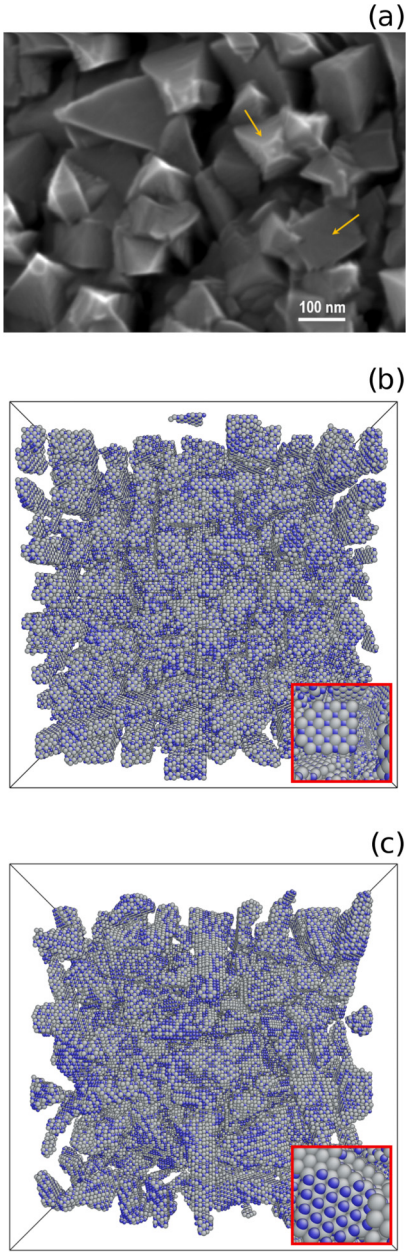

FIG. 4. Top-view SEM micrograph of a magnetron sputtered TiN film at 750 K (a), exhibiting faceted columns (arrows indicate local surfaces with either fourfold or threefold symmetry), compared with KMC simulation results obtained using diffusion model 1 (b) and model 2 (c). Simulated images (b,c) correspond to the top views of Figs. 3(c) and 3(f), respectively, and the insets inside are taken along the normal of the local surface, corresponding to (001)- and (111)-oriented surface, respectively (see Ref. [76]).

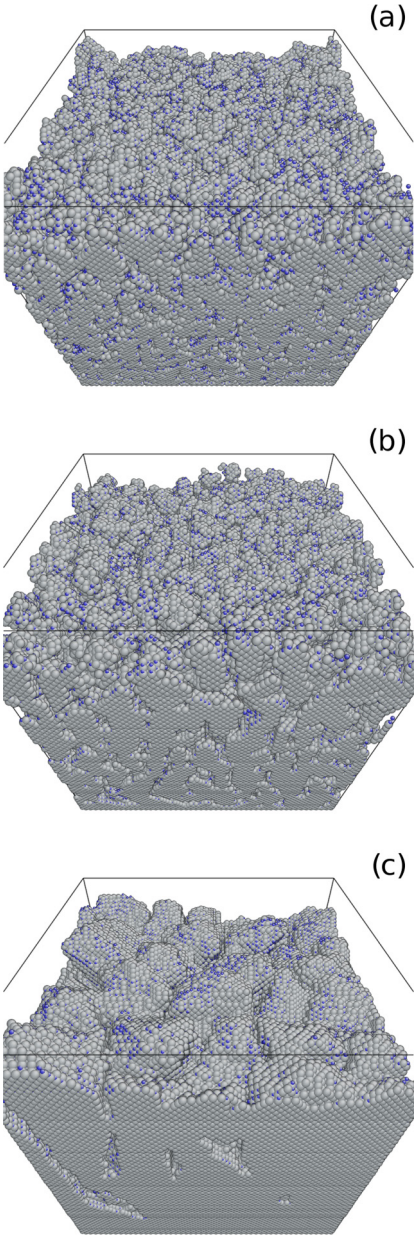

FIG. 5. Snapshots of the simulated TiN film growth structures corresponding to diffusion model 2 at $F = 1\,\mathrm{ML/s}$, $N_{\mathrm{nn}}^{\mathrm{min}} = 1$ and $N_{\mathrm{nnn}}^{\mathrm{min}} = 3$, $r_0 = \sqrt{2}$, and different temperatures: (a) $T = 300\,\mathrm{K}$, (b) $T = 400\,\mathrm{K}$, and (c) $T = 500\,\mathrm{K}$. The simulation box dimensions are $N_x = N_y = N_z = 100$ (see Ref. [76]).

physical vapor deposition of a thin film which takes place far from equilibrium and involves the formation of rough surfaces. Dynamic scaling theory [67,68], based on the concepts of scale invariance and fractals, is an effective approach to characterize the temporal evolution of the growing interface. Assuming a self-affine surface, different scaling exponents can be obtained to characterize the surface morphology. Typically, they can be extracted from the height difference correlation function $G(\boldsymbol{r})$ or interface width w. The scaling hypothesis requires that $G(r) \sim r^{2\alpha}$ for $r \ll \xi$ and $G(r) \sim 2w^2$ for $r \gg \xi$, where ξ is the lateral correlation length and α the roughness exponent. The growth exponent β is obtained through the power-law dependence of the interface width with time, $w \sim t^{\beta}$, before saturation is reached at later stages, while the correlation length grows as $\xi \sim t^{1/z}$, where $1/z$ is the dynamic exponent. The dynamic scaling theory predicts that $z = \alpha/\beta$, which has been found to be valid in many situations.

It is also known that polycrystalline films produced by sputtering techniques often develop columnar structures, when adatom mobility is relatively low, such as for TMN films. The surface profile exhibits a mountain landscape with hills and

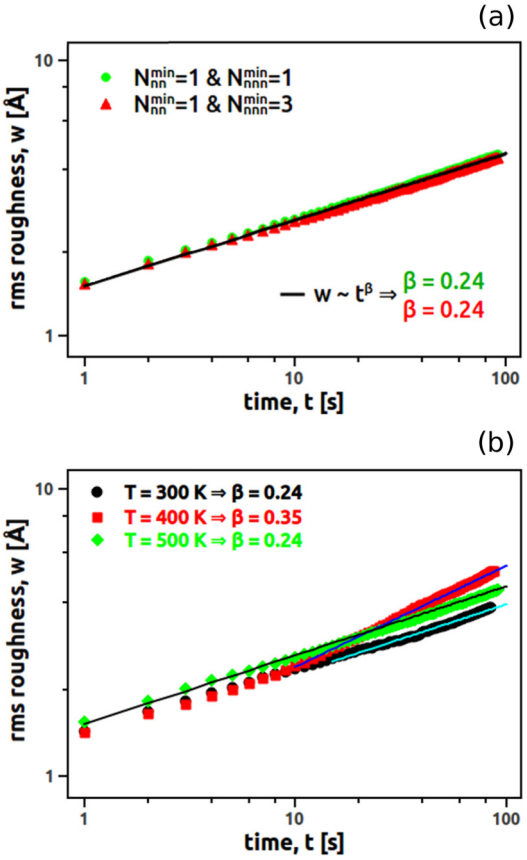

FIG. 6. (a) Time evolution of the rms surface roughness w of TiN film corresponding to diffusion model 2 at $F = 1\text{ML/s}$, $T = 500\,\text{K}$, and $r_0 = \sqrt{2}/2$. The solid line is a power-law fit of data, yielding a similar growth exponent $\beta = 0.24$ for $N_{nn}^{min} = 1$ and $N_{nnn}^{min} = 1$, and $N_{nn}^{min} = 1$ and $N_{nnn}^{min} = 3$. Simulation results are averaged from ten independent simulation runs to obtain smooth profiles. (b) Time evolution of the rms surface roughness w of TiN films deposited at different substrate temperatures, using diffusion model 2 at $F = 1\,\text{ML/s}$, $N_{nn}^{min} = 1$ and $N_{nnn}^{min} = 3$, and $r_0 = \sqrt{2}/2$. The solid lines are a power-law fit of data. Simulation results are averaged from ten independent simulation runs to obtain smooth profiles. The standard deviation of β exponent is 0.04, 0.01, and 0.01 at 300, 400, and 500 K, respectively.

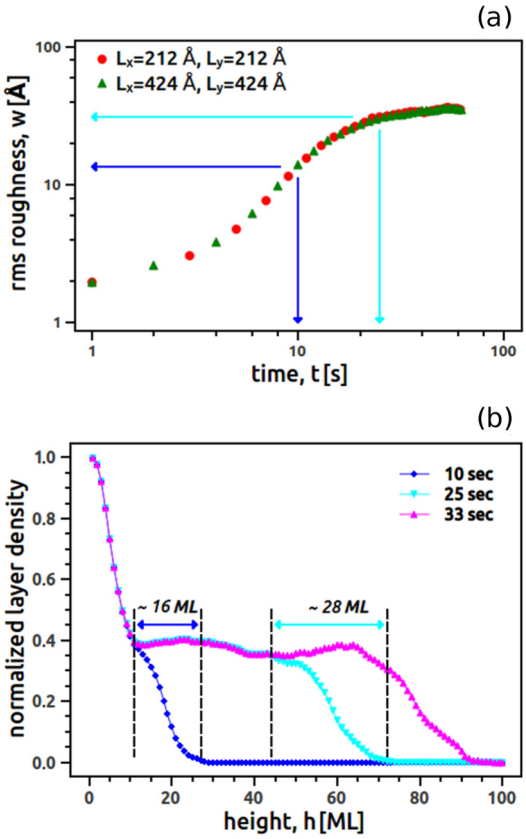

FIG. 7. Time dependence of the rms surface roughness (a) and its connection with the time evolution of the growth front width extracted from the final part of the normalized layer density curves (b). The results have been obtained using diffusion model 2 at $F = 1\,\text{ML/s}$, $T = 500\,\text{K}$, with $r_0 = 2\sqrt{2}$ and $N_{nn}^{min} = 1$ and $N_{nnn}^{min} = 3$. Data are reported in (a) for different simulation box dimensions. Data obtained after 33 s are also shown in (b) to better reveal the normalized layer density plateau ($\rho \sim 0.4$) reflecting the "volume" density of the film.

valleys, as a result of the angular distribution of the incoming particle flux and shadowing effects. In this situation the growth front is more complex, including overhangs and open voids, and the surface height $h(\boldsymbol{r},t)$ is no longer univocally defined. The presence of a mounded surface is an example for which the relation $z = \alpha/\beta$ is claimed to no longer hold [56].

We first examine the temporal evolution of the surface morphology of dense TiN films, such as those corresponding to Fig. 3(d), i.e., at relatively high temperature ($T = 500\,\text{K}$) and high deposited energy ($r_0 = \sqrt{2}/2$), and characterized by a compactness parameter $C \sim 1$. The rms surface roughness w is plotted against deposition time in Fig. 6(a) for two surface contact rules using diffusion model 2. A power-law dependence is clearly obtained, with a growth exponent $\beta \sim 0.24$ in both cases. This value is relatively low and attests for the development of a smooth surface under these growth conditions. It is close to the value $\beta = 0.25$ obtained from a random deposition model with relaxation (RDR) [68], the case of a purely stochastic growth (random deposition without relaxation) yielding $\beta = 0.5$. In the framework of the RDR model, the roughness is expected to saturate at longer times with a size-dependent steady-state value, which scales as $w \sim L^{\alpha}$ with $\alpha = 0.5$, L being the in-plane system dimension. A value of $\beta \sim 0.25$ was also reported by Hu *et al.* [69] from KMC modeling of the growth of porous silicon layers. These authors also observed a steady-state value of the roughness at large times, from which they extracted a roughness exponent value $\alpha = 0.5$. Such saturation phenomenon is not observed in Fig. 6(a), but there are situations in which this behavior is reproduced [see Fig. 7(a)]. The relatively low value of $\beta = 0.24$ found at $T = 500\,\text{K}$ can be related to the surface diffusion processes that our KMC model takes into account and which are thermally activated at this temperature. A decrease of β with increasing number of diffusing surface atoms per incident deposited particle has been reported by Karabacak *et al.* [44] from KMC simulations in which surface diffusion, but also reemission, were taken into account. A recent study by Alvarez *et al.* confirmed this tendency [56], a lowest value of

$\beta = 0.15$ being obtained for ZrO_2 films in the growth regime dominated by surface diffusion. Surface diffusion, together with evaporation, are known as relaxation processes and contribute to a smoothening of the surface topography [70]. Das Sarma and Tamborenea [71] proposed a kinetic growth model, representative of molecular beam epitaxy conditions, where $\beta \sim 0.38$, that accounts for relaxation of atoms via hopping towards the nearest kink site. Our diffusion model 2 includes such processes since the diffusion towards sites with higher coordination number corresponds to lower values of the activation energy; i.e., atoms can diffuse to the nearest local energy minima.

Our computed value of β is also in fairly good agreement with experimental data of Liu *et al.* [72] on polycrystalline TiN films ($\beta = 0.28$) and Karr *et al.* [73] on single-crystal, epitaxial TiN films ($\beta = 0.25$) deposited by magnetron sputtering.

The influence of substrate temperature on the time evolution of surface roughness of TiN films is displayed in Fig. 6(b) for $N_{nn}^{min} = 1$ and $N_{nnn}^{min} = 3$ and $r_0 = \sqrt{2}/2$ deposition conditions. The same regime is observed in the initial growth stages ($t < 10$ s), while different growth exponents can be extracted at larger deposition times. The highest roughness is obtained at $T = 400$ K, corresponding also to a larger value of $\beta = 0.35$, comparatively to the values of 0.24 found at T = 300 and 500 K. A nonmonotonous evolution of the surface roughness with substrate temperature was also reported by Hu *et al.* [69], evidencing a crossover behavior with increasing temperature (in their case, the roughness reached a maximum value at $T = 600$ K). This reflects competition between different surface diffusion driven processes, namely particles aggregation (being firstly effective) and surface smoothening (favored at higher temperatures).

We have shown in Sec. III A that increasing the value of the interaction parameter r_0 yields the development of rougher TiN surfaces (see also Table II). One illustration is provided in Fig. 7(a), results obtained at $r_0 = 2\sqrt{2}$, where it can be clearly seen that the interface width starts to saturate after $t \sim 25$ s, reaching a steady-state value of ~40 Å. Before reaching saturation, the roughness increases with time following a power law, and we can extract a growth exponent $\beta = 1.4$ (between $t = 6$ and 15 s). It is interesting to analyze these results based on the density profile, as shown in Fig. 7(b). The normalized layer density $\rho(z,t)$ decreases in a nonmonotonous way along the growth direction. In particular, after 25 s of deposition the maximum height corresponds to 75 ML, due to the formation of voids and overhangs. The compactness C of this film is found to be equal to 0.65 in the case of $N_{nn}^{min} = 1$ and $N_{nnn}^{min} = 3$ (see Table II). If one analyzes the data obtained after $t = 25$ s [corresponding to the cyan curve in Fig. 7(b)], one observes a rapid decrease of $\rho(z,t)$ from 1 (at the substrate interface) to 0.4 (at a height z corresponding to ~10 ML), followed afterwards by a density plateau, $\rho(z,t) \sim 0.4$, between 10 and 45 ML, the upper region between 45 and 75 ML corresponding to the interface with the vacuum (i.e., the growth front). The width of this interface is ~28 ML, in good agreement with the rms roughness value deduced from Fig. 7(a) (note that the width of this upper region corresponds to $2w$). Therefore, the plot of density profiles can be used as a tool to derive the rms roughness, similarly to what has been reported in the work of Wang and Clancy [45]. The plateau observed below the growth front in Fig. 7(b) reflects the "volume" density of the film. This density plateau becomes visible above 10 deposited MLs of TiN, and is preserved afterwards with increasing deposition time [see Fig. 8(a)]. This is typical of a columnar growth and reflects shadowing effects, as illustrated in Fig. 8(b). For $r_0 = 2\sqrt{2}$, incoming particles can stick more effectively to existing surfaces. When some columns start to grow, they intercept a higher fraction of the incoming flux, while the surrounding valleys are deprived from incoming particles. As a result of the formation of inclined columns and overhangs, some columns start to be shadowed, such as the one marked with an arrow in Fig. 8(b). It is interesting to note that the largest growth exponent corresponds to this regime. The obtained value of $\beta = 1.4$ is relatively high but in good agreement with models where shadowing effect is the dominant mechanism ($\beta = 1$) [44,56,70,74]. Thus shadowing effect plays an important role in kinetic roughening of TiN thin films, while thermally activated surface diffusion tends to smoothen the surface. Note that shadowing manifests only after a certain amount of deposited material, as incoming particles manage to reach flat surfaces (substrate or 2D islands) in the early growth stages, which explains the relatively higher layer density values close to the substrate interface.

The influence of the r_0 parameter on the resulting film porosity (quantified as $1-C$) is shown in Fig. 9, for different substrate temperatures. One can see that the film porosity decreases, as expected, with increasing temperature as thermally activated surface diffusion processes lead to film densification. Increasing the value of r_0 yields the development of more porous TiN film microstructures, due to more predominant shadowing effect.

Figure 10(a) shows the square root of the height difference correlation function, $G^{1/2}(r)$, extracted at different film thickness for the same deposition conditions as those in Fig. 6(a), i.e., for a fully dense TiN film deposited at $F = 1$ ML/s, $T = 500$ K, and $r_0 = \sqrt{2}/2$. The log-log plots shown in Fig. 10(a) are averaged over several deposition runs to increase statistics. The curves exhibit a linear regime, $G^{1/2}(r) \sim r^{\alpha}$ for $r \ll \xi$, from which the roughness exponent α can be extracted, and at larger distances a saturation is reached. A value of $\alpha \sim 0.72$ is obtained for the thicker films, a slightly lower value being deduced for film thickness under 10 ML, likely due to nonstationary growth at early stages [44]. This is confirmed by the fact that the curves do not perfectly overlap until the deposition times reach 10 s. According to the scaling theory, the interface width can be extracted from the saturation region at large r values, where $G^{1/2}(r) \approx \sqrt{2}w$. The values of w extracted from the plateau in the $G^{1/2}(r)$ curves are in excellent agreement with the rms roughness calculated from Eq. (2)—e.g., for $t = 90$ s one obtains $w \sim 4.4$ Å, close to the value reported in Table II—and the time dependence yields the same growth exponent $\beta = 0.24$ as that obtained from Fig. 6(a). One can also notice in Fig. 10(a) the presence of a local minimum in the saturation region of the height difference correlation function. This is characteristic of the existence of mounded surfaces, and the average mound separation, d, can be extracted from the location of this minimum [56,73,75]. The trends manifested by the $G(r)$ function are therefore consistent with the visual inspection of the surface topography of Fig. 3(d), where mounds with typical length of 5 nm were formed after

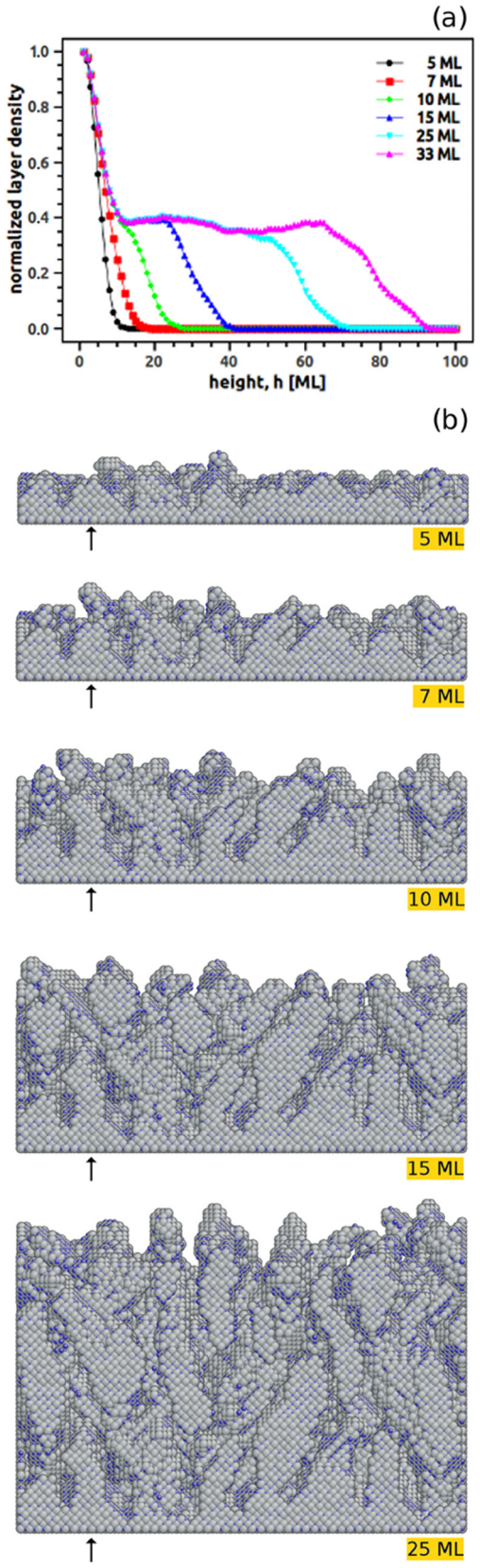

FIG. 8. Time evolution of normalized layer density (a) and sequential snapshots (cross-sectional view) shown up to 25 ML of TiN deposited structure showing shadowing effect (b). The results have been obtained using diffusion model 2 at $F = 1$ ML/s, $T = 500$ K, with $r_0 = 2\sqrt{2}$ and $N_{\rm nn}^{\rm min} = 1$ and $N_{\rm nnn}^{\rm min} = 3$ (see Ref. [76]).

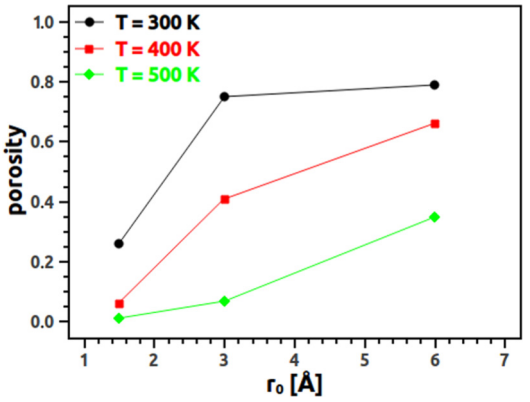

FIG. 9. Influence of substrate temperature and interaction parameter r_0 on the resulting TiN film porosity. The results have been obtained using diffusion model 2 at $F = 1$ ML/s and $N_{\rm nn}^{\rm min} = 1$ and $N_{\rm nnn}^{\rm min} = 3$.

90 s. The evolution of d with increasing deposition time is reported in Fig. 10(b): a power-law dependence is found, with a coarsening exponent $p \sim 0.23$. This value is the same, within statistical error, as that obtained for the growth exponent β deduced from Fig. 6(a). Similar findings, $p \sim \beta \sim 0.25$ and $\alpha \sim 0.5$, have been reported experimentally by Karr *et al.* [73] in single-crystal TiN(001) films. In their case, the lower value of α, together with larger mounds' lateral size (>100 nm), may be accounted for by the higher deposition temperatures

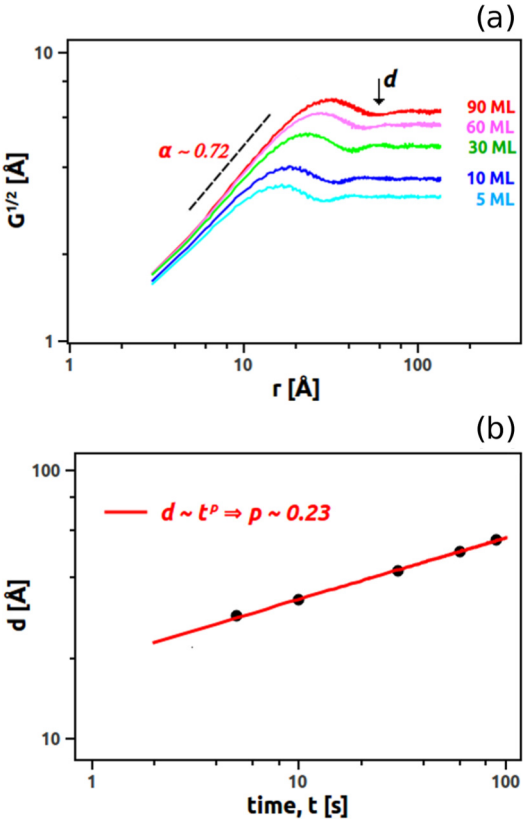

FIG. 10. (a) Square root of the height-difference correlation function $G^{1/2}(r)$ for TiN film growth at different thickness (in ML) using same deposition conditions as those in Fig. 6(a). (b) The average mound separation, d, as a function of deposition time.

(1023 K) compared to the present KMC results (500 K). If we assume that the scaling hypothesis is valid, then the relation $p = 1/z = \beta/\alpha$ should be fulfilled. In the present case, this yields $1/z = 0.33$, which is in a reasonable agreement with the computed value of the coarsening exponent p. Under the chosen deposition conditions [Fig. 3(d)], shadowing effect is minimized as the r_0 parameter is relatively small, which would reflect more energetic deposition conditions, e.g., at low working pressure or with the application of a substrate bias voltage, resulting in smooth surface morphology and pervading a self-affine structure.

IV. CONCLUSIONS

We have proposed and implemented a 3D kinetic Monte Carlo model for thin film deposition of transition metal nitrides, with conditions intended to approximate the reactive magnetron sputter deposition. The model is first applied to the case of the TiN system, chosen as a model compound with cubic (NaCl-type) structure. At this stage, the model based on a single rigid lattice, with one predefined crystallographic orientation, includes both diffusion and deposition processes. It is capable of predicting a wide variety of TiN growth morphologies, including the formation of tilted columns, overhangs, and voids, as well as surface faceting.

We have investigated the influence of the deposition parameters, such as the substrate temperature and deposition rate, as well as two different surface diffusion models, on the resulting film microstructures at normal incidence and equal flux of N and Ti atoms. The deposition model involves an interaction parameter r_0, equivalent to a capture length, which mimics the probability for incoming particles to stick on an existing surface. At low temperature ($T = 300$ K) and large value of r_0, the growth mode is characteristic of a "hit and stick" ballistic deposition, and films with a high degree of porosity (compactness <0.25) are obtained. At high temperature ($T = 500$ K) and low value of r_0, fully dense TiN films with smooth surface are produced due to the predominance of thermally activated surface diffusion events. Increasing the value of r_0 favors the formation of rough surfaces and the development of overhangs and voids, as a result of shadowing effect. The formation of different crystallographic facets is well reproduced by the simulations, in qualitative accordance with experimental findings. Surface faceting is a direct consequence of the diffusion model which includes an intrinsic (minimum energy-based) diffusion anisotropy, although no crystallographic diffusion anisotropy was explicitly included in the model.

The temporal evolution of the interface width yields a growth exponent $\beta = 0.24$ and a roughness exponent $\alpha = 0.72$, as deduced from the height difference correlation function, for the case of fully dense films, in good agreement with existing experimental data on epitaxial TiN(001) films.

The present model does not take into account the diffusion of TiN_x aggregates with $x \geqslant 1$, N_2 desorption, nor the creation of point defects (interstitial or substitutional) due to film bombardment by hyperthermal incoming particles. However, the effect of deposited energy is seemingly captured by the use of the r_0 parameter, at least qualitatively. The model can also implement different angular distributions of the incoming particles, matching the real sputter-deposition conditions or a predefined oblique incidence. It can also be readily extended to treat the case of ternary alloys, which finds general implication in the prospects of microstructure tailoring by alloying or interface design in TMN systems.

ACKNOWLEDGMENTS

This work has been performed within the M.ERA-NET project MC^2 "Multi-scale Computational-driven design of novel hard nanostructured Coatings" and funded by the French ANR program (Project No. ANR-13-MERA-0002-02). It also belongs to the French Government program "Investissements d'Avenir" (LABEX INTERACTIFS, Reference No. ANR-11-LABX-0017-01) granted to P′ Institute.

[1] W. D. Sproul, Science **273**, 889 (1996).
[2] G. M. Matenoglou, L. E. Koutsokeras, and P. Patsalas, Appl. Phys. Lett. **94**, 152108 (2009).
[3] L. E. Koutsokeras, G. Abadias, Ch. E. Lekka, G. M. Matenoglou, D. F. Anagnostopoulos, G. A. Evangelakis, and P. Patsalas, Appl. Phys. Lett. **93**, 011904 (2008).
[4] T. Seppänen, L. Hultman, and J. Birch, Appl. Phys. Lett. **89**, 181928 (2006).
[5] S. Mahieu, W. P. Leroy, K. Van Aeken, M. Wolter, J. Colaux, S. Lucas, G. Abadias, P. Matthys, and D. Depla, Solar Energy **85**, 538 (2011).
[6] P. Patsalas, N. Kalfagiannis, and S. Kassavetis, Materials **8**, 3128 (2015).
[7] S-H. Jhi, S. G. Louie, M. L. Cohen, and J. Ihm, Phys. Rev. Lett. **86**, 3348 (2001).
[8] S. K. R. Patil, N. S. Mangale, S. V. Khare, and S. Marsillac, Thin Solid Films **517**, 824 (2008).
[9] B. D. Fulcher, X. Y. Cui, B. Delley, and C. Stampfl, Phys. Rev. B **85**, 184106 (2012).
[10] L. Hultman, Vacuum **57**, 1 (2000).
[11] A. Hoerling, J. Sjölen, H. Willman, T. Larsson, M. Oden, and L. Hultman, Thin Solid Films **516**, 6421 (2008).
[12] H. Lind, R. Forsén, B. Alling, N. Ghafoor, F. Tasnadi, M. P. Johansson, I. A. Abrikosov, and M. Odén, Appl. Phys. Lett. **99**, 091903 (2011).
[13] G. Aschermann, E. Friedrich, E. Justi, and J. Kramer, Phys. Z. **42**, 349 (1941).
[14] A. B. Mei, A. Rockett, L. Hultman, I. Petrov, and J. E. Greene, J. Appl. Phys. **114**, 193708 (2013).
[15] D. G. Sangiovanni, V. Chirita, and L. Hultman, Phys. Rev. B **81**, 104107 (2010).
[16] D. Holec, L. Zhou, R. Rachbauer, and P. H. Mayrhofer, J. Appl. Phys. **113**, 113510 (2013).
[17] V. Petrman and J. Houska, J. Mater. Sci. **48**, 7642 (2013).
[18] G. Abadias, M. B. Kanoun, S. Goumri-Said, L. Koutsokeras, S. N. Dub, and Ph. Djemia, Phys. Rev. B **90**, 144107 (2014).
[19] P. H. Mayrhofer, C. Mitterer, L. Hultman, and H. Clemens, Prog. Mater. Sci. **51**, 1032 (2006).

[20] J. Patscheider, N. Hellgren, R. T. Haasch, I. Petrov, and J. E. Greene, Phys. Rev. B **83**, 125124 (2011).

[21] H. Kindlund, D. G. Sangiovanni, L. Martinez-de-Olcoz, J. Lu, J. Jensen, J. Birch, I. Petrov, J. E. Greene, V. Chirita, and L. Hultman, APL Mater. **1**, 042104 (2013).

[22] N. Ghafoor, L. S. Johnson, D. O. Klenov, J. Demeulemeester, P. Desjardins, I. Petrov, L. Hultman, and M. Odén, APL Mater. **1**, 022105 (2013).

[23] G. Abadias, L. E. Koutsokeras, A. Siozios, and P. Patsalas, Thin Solid Films **538**, 56 (2013).

[24] N. Ghafoor, I. Petrov, D. O. Klenov, B. Freitag, J. Jensen, and J. E. Greene, Acta Mater. **82**, 179 (2015).

[25] S. Veprek, M. G. J. Veprek-Heijman, P. Karvankova, and J. Prochazka, Thin Solid Films **476**, 1 (2005).

[26] P. B. Barna and G. Radnoczi, in *Metallic Films for Electronic, Optical and Magnetic Applications*, edited by K. Barmak and K. Coffey (Woodhead Publishing Ltd., Oxford, 2014), p. 67.

[27] S. Nagao, K. Nordlund, and R. Nowak, Phys. Rev. B **73**, 144113 (2006).

[28] D. Holec, M. Friak, J. Neugebauer, and P. H. Mayrhofer, Phys. Rev. B **85**, 064101 (2012).

[29] F. Tasnadi, M. Odén, and I. A. Abrikosov, Phys Rev B **85**, 144112 (2012).

[30] N. Schell, W. Matz, J. Bottiger, J. Chevalier, and P. Kringhoj, J. Appl. Phys. **91**, 2037 (2002).

[31] L. Székely, G. Safran, V. Kis, Z. E. Horváth, P. H. Mayrhofer, M. Moser, G. Radnóczi, F. Misják, and P. B. Barna, Surf. Coat. Technol. **257**, 3 (2014).

[32] K. Sarakinos, J. Alami, and S. Konstantinidis, Surf. Coat. Technol. **204**, 1661 (2010).

[33] A. P. Ehiasarian, A. Vetushka, Y. A. Gonzalvo, G. Sáfrán, L. Székely, and P. B. Barna, J. Appl. Phys. **109**, 104314 (2011).

[34] S. Mahieu, P. Ghekiere, D. Depla, and R. De Gryse, Thin Solid Films **515**, 1229 (2006).

[35] S. Mahieu and D. Depla, J. Phys. D: Appl. Phys. **42**, 053002 (2009).

[36] D. Gall, S. Kodambaka, M. A. Wall, I. Petrov, and J. E. Greene, J. Appl. Phys. **93**, 9086 (2003).

[37] M. Marlo and V. Milman, Phys. Rev. B **62**, 2899 (2000).

[38] G. Abadias, W. P. Leroy, S. Mahieu, and D. Depla, J. Phys. D: Appl. Phys. **46**, 055301 (2013).

[39] R. Daniel, E. Jäger, J. Todt, B. Sartory, C. Mitterer, and J. Keckes, J. Appl. Phys. **115**, 203507 (2014).

[40] S. Mahieu, D. Depla, and R. De Gryse, Surf. Coat. Technol. **202**, 2314 (2008).

[41] G. Greczynski, J. Lu, J. Jensen, I. Petrov, J. E. Greene, S. Bolz, W. Kölker, Ch. Schiffers, O. Lemmer, and L. Hultman, Thin Solid Films **556**, 87 (2014).

[42] H. Huang, G. H. Gilmer, and T. Díaz de la Rubia, J. Appl. Phys. **84**, 3636 (1998).

[43] P. Bruschi, A. Nannini, and F. Pieri, Phys. Rev. B **63**, 035406 (2000).

[44] T. Karabacak, Y.-P. Zhao, G. C.-C. Wang, and T.-M. Lu, Phys. Rev. B **64**, 085323 (2001).

[45] L. Wang and P. Clancy, Surf. Sci. **473**, 25 (2001).

[46] A. Yanguas-Gil, J. Cotrino, A. Barranco, and A. R. Gonzalez-Elipe, Phys. Rev. Lett. **96**, 236101 (2006).

[47] S. Lucas and P. Moskovkin, Thin Solid Films **518**, 5355 (2010).

[48] J. Dalla Torre, G. H. Gilmer, D. L. Windt, R. Kalyanaraman, F. H. Baumann, P. L. O'Sullivan, J. Sapjeta, T. Diaz de la Rubia, and M. Djafari Rouhani, J. Appl. Phys. **94**, 263 (2003).

[49] D. G. Sangiovanni, D. Edström, L. Hultman, V. Chirita, I. Petrov, and J. E. Greene, Phys. Rev. B **86**, 155443 (2012).

[50] J. P. Biersack and L. Haggmark, Nucl. Instrum. Methods **174**, 257 (1980), see also http://www.srim.org

[51] K. Van Aeken, S. Mahieu, and D. Depla, J. Phys. D.: Appl. Phys. **41**, 205307 (2008), see also http://www.draft.ugent.be/

[52] F. Family and T. Vicsek, *Dynamics of Fractal Surfaces* (World Scientific, Singapore, 1991).

[53] G. Abadias, V. I. Ivashchenko, L. Belliard, and Ph. Djemia, Acta Mater. **60**, 5601 (2012).

[54] J. E. Rubio, M. Jaraiz, I. Martin-Bragado, J. M. Hernandez-Mangas, J. Barbolla, and G. H. Gilmer, J. Appl. Phys. **94**, 163 (2003).

[55] J. B. Adams, Z. Wang, and Y. Li, Thin Solid Films **365**, 201 (2000).

[56] R. Álvarez, A. Palmero, L. O. Prieto-López, F. Yubero, J. Cotrino, W. de la Cruz, H. Rudolph, F. H. P. M. Habraken, and A. R. Gonzalez-Elipe, J. Appl. Phys. **107**, 054311 (2010).

[57] P. Bruschi, A. Nannini, and M. Piotto, Comput. Mater. Sci. **17**, 299 (2000).

[58] G. H. Gilmer and P. Bennema, J. Appl. Phys. **43**, 1347 (1972).

[59] F. Montalenti and R. Ferrando, Phys. Rev. B **59**, 5881 (1999).

[60] Y. Ren, X. Liu, X. Tan, and E. Westkämper, Comput. Mater. Sci. **77**, 102 (2013).

[61] C. Tholander, B. Alling, F. Tasnadi, J. E. Greene, and L. Hultman, Surf. Sci. **630**, 28 (2014).

[62] D. Edström, D. G. Sangiovanni, L. Hultman, V. Chirita, I. Petrov, and J. E. Greene, Thin Solid Films **558**, 37 (2014).

[63] D. G. Sangiovanni, D. Edström, L. Hultman, I. Petrov, J. E. Greene, and V. Chirita, Surf. Sci. **627**, 34 (2014).

[64] R. Alvarez, C. Lopez-Santos, J. Parra-Barranco, V. Rico, A. Barranco, J. Cotrino, A. R. Gonzalez-Elipe, and A. Palmero, J. Vac. Sci. Technol. B **32**, 041802 (2014).

[65] X. W. Zhou and H. N. G. Wadley, Surf. Sci. **431**, 42 (1999).

[66] L. A. Zepeda-Ruiz, E. Chason, G. H. Gilmer, Y. Wang, H. Xu, A. Nikroo, and A. V. Hamza, Appl. Phys. Lett. **95**, 151910 (2009).

[67] D. E. Wolf and J. Villain, Europhys. Lett. **13**, 389 (1990).

[68] F. Family, Physica A **168**, 561 (1990).

[69] G. Hu, J. Huang, G. Orkoulas, and P. D. Christofides, Phys. Rev. E **80**, 041122 (2009).

[70] J. H. Yao and H. Guo, Phys. Rev. E **47**, 1007 (1993).

[71] S. Das Sarma and P. Tamborenea, Phys. Rev. Lett. **66**, 325 (1991).

[72] Z.-J. Liu, N. Jiang, Y. G. Shen, and Y.-W. Mai, J. Appl. Phys. **92**, 3559 (2002).

[73] B. W. Karr, I. Petrov, D. G. Cahill, and J. E. Greene, Appl. Phys. Lett. **70**, 1703 (1997).

[74] J. T. Drotar, Y.-P. Zhao, T.-M. Lu, and G.-C. Wang, Phys. Rev. B **62**, 2118 (2000).

[75] A. B. Mei, B. M. Howe, C. Zhang, M. Sardela, J. N. Eckstein, L. Hultman, A. Rockett, I. Petrov, and J. E. Greene, J. Vac. Sci. Technol. A **31**, 061516 (2013).

[76] All snapshots shown in the paper have been obtained using AtomEye free visualization software, J. Li, Model. Simul. Mater. Sci. Eng. **11**, 173 (2003).